RSC Advances

PAPER

View Article Online
View Journal | View Issue

Cite this: *RSC Adv.*, 2026, **16**, 16841

Replicating the post-chemotherapy tumor microenvironment *via* biomimetic scaffolds to regulate MSC differentiation

Zhe Fan, [ade] Huiying Zhang,[b] Lulu Wang,*[c] Jinxiang Tian,[a] Huaiqing Jiang,[d] Yazhou Chen, [*d] Biao Guo[a] and Haiyang Yu*[a]

Received 5th February 2026
Accepted 16th March 2026

DOI: 10.1039/d6ra01031h

rsc.li/rsc-advances

The repair of tumor-induced bone defects requires regenerative materials capable of functioning within the harsh conditions of cancer therapy. Herein, we introduce a biomimetic scaffold designed to simulate the post-chemotherapy tumor microenvironment to investigate its specific effects on tissue regeneration. The scaffold features a PLGA knitted mesh/collagen sponge hybrid loaded with mineralized, DOX-carrying mesoporous silica nanoparticles (DOX-MSNCaP). The sustained release of DOX facilitates potent tumor cell elimination, thereby establishing a residual post-chemotherapy microenvironment. We subsequently explored the biological response of mesenchymal stem cells (MSCs) to this specific biomimetic environment. Our results indicate that the scaffold significantly enhances MSC adhesion and drives osteogenic differentiation through the upregulation of YAP/TAZ signaling. Overall, these findings suggest that following tumor eradication, the scaffold effectively facilitates MSC-mediated osteogenesis, serving as a promising therapeutic strategy for post-tumor bone reconstruction.

1 Introduction

Osteosarcoma (OS) is the most prevalent primary malignant bone tumor, predominantly affecting children and adolescents.[1,2] The impact of OS is profound, often leading to lifelong disability or fatality and imposing a significant socioeconomic burden.[3,4] While surgical resection remains the standard of care, it frequently results in critical-sized bone defects that exceed the body's innate regenerative capacity. Furthermore, the complete eradication of tumor cells is clinically challenging, with local recurrence rates reported in approximately 90% of patients.[5,6] Although adjuvant chemotherapy and radiotherapy are employed to eliminate residual cancer cells, these systemic treatments are associated with severe toxicities and off-target side effects that drastically compromise patient quality of life.[7,8]

Recent advancements in tissue engineering and localized cancer therapy have driven the development of biodegradable implants for post-operative management.[9–13] These multifunctional scaffolds aim to integrate tumor inhibition with tissue regeneration. For instance, various bioactive scaffolds functionalized with photothermal nanomaterials, such as Fe_3O_4 nanoparticles,[12] MoS_2 nanosheets,[14] and functioned nanofiber membranes,[15] have been developed. Chen *et al.* also developed bifunctional scaffolds based on gelatin and black phosphorus nanosheets, which exhibited notable anti-cancer effects against breast cancer cells and promoted MSC adipogenic differentiation.[16] Similarly, Song *et al.* reported a 3D-printed scaffold that combined photothermal therapy (PTT) and chemotherapy to effectively suppress tumor growth.[17] Collectively, these platforms have demonstrated remarkable *in vivo* efficacy in reducing OS cell viability while supporting the proliferation and osteogenic differentiation of mesenchymal stem cells (MSCs).

Clinically, however, post-operative tumor treatment and tissue regeneration are sequential events rather than simultaneous processes. Consequently, a critical gap remains in understanding whether the residual microenvironment, specifically the extracellular matrix (ECM) altered by chemotherapy-induced tumor cell death, remains permissive for the subsequent proliferation and differentiation of MSCs. Most existing studies overlook this temporal distinction, treating tumor elimination and bone regeneration as isolated functional goals. Bridging this gap is crucial, as post-surgical regeneration inevitably occurs within this specific post-therapeutic microenvironment.

To address this, the integration of stimuli-responsive nanocarriers into scaffolds offers a promising approach. Mesoporous

[a]*Department of Orthopedics, Affiliated Fuyang People's Hospital of Anhui Medical University, National Key Clinical Specialty, Clinical Research Center for Spinal Deformity of Anhui Province, Fuyang, Anhui Province 236000, China. E-mail: fy.yhy@163.com*

[b]*Henan Provincial Chest Hospital, The Chest Hospital of Zhengzhou University, Zhengzhou 450006, China*

[c]*Department of Plastic Surgery, The Third People's Hospital of Henan Province, Zhengzhou 450007, Henan, China. E-mail: luna0323@163.com*

[d]*Henan Institute of Advanced Technology, Zhengzhou University, Zhengzhou 450003, PR China. E-mail: yzchenbio@zzu.edu.cn*

[e]*Department of Orthopedic Surgery, The First Affiliated Hospital of Zhengzhou University, Zhengzhou 450042, China*

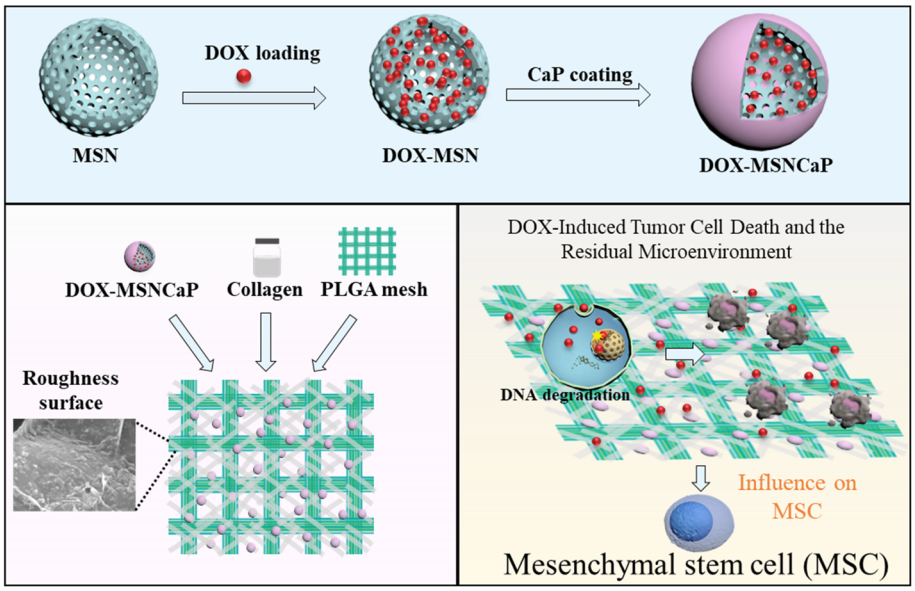

Scheme 1 Schematic illustration of the preparation of DOX-MSNCaP@PLGA-collagen scaffolds for recapitulating the post-chemotherapy microenvironment and regulating cell differentiation.

silica nanoparticles (MSNs) have emerged as superior inorganic nanocarriers due to their high drug-loading capacity, stability, and biocompatibility.[18–21] Specifically, MSNs mineralized with calcium and phosphate (MSNCaP) can serve as pH-responsive vehicles. While MSNCaP has been used for nitric oxide delivery,[22,23] it is also an ideal candidate for encapsulating doxorubicin (DOX) to achieve acid-triggered release in the tumor microenvironment. Compared to uncoated MSNs that typically exhibit rapid and non-specific burst release, the CaP shell functions as a robust gatekeeper to seal the mesopores at physiological pH, allowing for subsequent dissolution and targeted DOX release specifically within acidic environments.[24,25] Structurally, while collagen is highly biocompatible,[26–29] its mechanical limitations necessitate reinforcement. In our previous research, we successfully engineered a hybrid scaffold combining synthetic poly(DL-lactic-*co*-glycolic acid) (PLGA) with collagen, achieving excellent mechanical strength and biocompatibility,[30] and we have validated its ability to support MSC osteogenesis.[31,32]

Herein, we aim to construct a biomimetic scaffold that simulates the "post-chemotherapy tumor microenvironment" to investigate its specific regulatory effect on bone regeneration. To achieve this, we fabricated a DOX-MSNCaP@PLGA-collagen bifunctional scaffold by hybridizing DOX-loaded MSNCaP with a PLGA mesh/collagen sponge. This system leverages pH-responsive drug release to facilitate potent tumor cell elimination. Crucially, we moved beyond simple bifunctionality to explore the biological response of MSCs within this specific post-treatment environment. The micro- and nanostructures, drug release profiles, and anti-osteosarcoma properties were characterized. Finally, we evaluated the effect of this hybrid system on MSC adhesion and osteogenesis (Scheme 1).

2 Materials and methods

2.1 Synthesis of mesoporous silica nanoparticles (MSNs) and MSNCaP

The MSNs were prepared based on a previous report with some modifications.[33] In brief, 240 mL of Milli-Q water and 1.75 mL of NaOH (1.7 M) were mixed at 40 °C, after that, 0.5 g *N*-cetyltrimethylammonium bromide (CTAB, 99%, Sigma Aldrich) was added to the system, followed by 30 minutes stirring. Then, the tetraethyl orthosilicate (TEOS, 98%, Sigma Aldrich) was added slowly to the reaction mixture and incubated for another 2 hours. After cooling to room temperature (RT), the samples were centrifuged (14 000 g, 20 minutes) and washed three times using a mixture of ethanol/water (50% v/v). The samples were further dried overnight to obtain nanoparticles. Finally, the CTAB was eliminated by subjecting the nanoparticles to a furnace at 550 °C for 6 hours, employing a heating rate of 10 °C min^{-1}. The obtained MSNs were stored at RT for further use.

To prepare MSNCaP, the process involved several steps. Firstly, MSNs were dispersed in MilliQ water. Subsequently, a solution containing $Ca(OH)_2$ (0.15 g L^{-1}) and DHP (0.10 g L^{-1}) was slowly added dropwise to the dispersion. The mixture was then stirred overnight at room temperature (RT). Afterward, the mixture underwent centrifugation at 14000 g for 20 minutes to obtain the MSNCaP nanoparticles. These nanoparticles were subsequently dried overnight at 50 °C.

2.2 Drug loading

The doxorubicin hydrochloride (DOX·HCl) was used to load onto MSN. Briefly, an aqueous solution of DOX (2 mg mL^{-1}) was mixed with MSNs dispersion (1 mg mL^{-1}). Then, the mixture was stirred at RT in dark for 72 hours to reach an equilibrium state, followed by centrifugation (14 000 g, 20 minutes) to

harvest DOX-loaded MSN (DOX-MSN). The DOX-MSN was further washed and centrifuged, meanwhile the supernatant and washing solutions were collected and measured by UV-vis absorbance at 483 nm. The drug loading capability was determined according to equation: the drug loading efficiency (DLE) and drug loading capacity (DLC) were calculated according to the following equations:

$$\text{DLE (\%)} = (\text{weight of loaded DOX/weight of initial DOX}) \times 100\%$$

$$\text{DLC (\%)} = (\text{weight of loaded DOX/weight of DOX-loaded nanoparticles}) \times 100\%$$

The weight of loaded DOX was determined by subtracting the weight of unloaded DOX in the supernatant from the total weight of initial DOX. The method of CaP coating on DOX-loaded MSN was same as described in materials methods "2.1 Synthesis of MSNCaP"

2.3 Preparation of PLGA-collagen and DOX-MSNCaP@PLGA-collagen hybrid mesh

A PLGA knitted mesh (a ratio of 90 : 10 for glycolic acid and lactic acid) used in this work was obtained from Biomedical Structures (Warwick, Rhode Island, USA). Each original sheet of PLGA mesh was 10.5 cm × 10.5 cm with a thickness of 200 μm. The mesh was sealed in a vacuum sleeve and stored at 4 °C until use. For the fabrication of PLGA-collagen hybrid mesh, a hybridization method was used according to our previous work.[34] Briefly, the PLGA mesh was used, and the acidic bovine collagen solution (1 wt%, type I, Koken Japan) was eluted on the mesh to fill the space of PLGA mesh. After removing the excess aqueous collagen solution, a thin layer of PLGA mesh/collagen construct was formed. The PLGA mesh/collagen constructs were followed by being frozen at −80 °C and frozen drying to allow the formation of collagen micro-sponges. After further EDC/NHS-cross-linking (a mixture of 0.05 M EDC and 0.02 M NHS), a glycine solution was added to block the crosslink reaction, followed by washing with Milli-Q water 3 times. The PLGA-collagen hybrid mesh was frozen-dried and stored at 4 °C for further use. The DOX-MSNCaP@PLGA-collagen hybrid meshes were prepared through freeze-dry and EDC/NHS-cross-liking method. The prepared conditions for collagen micro-sponges were the same as that for the PLGA-collagen mesh.

2.4 Release profiles of DOX

The release profiles of DOX were determined in PBS (pH = 7.4 or pH = 6.5) at 37 °C. In brief, the DOX-MSNCaP@PLGA-collagen meshes were placed in a dialysis bag (14 000 Da) and then the dialysis bag was immersed in a 50 mL tube containing 20 mL PBS buffer. The tube was further incubated in a shaker at 100 rpm and 37 °C. The release buffer was taken out from the tube at predetermined time intervals and was replaced with fresh PBS. Concentrations of the DOX in the released buffer were determined by UV-vis absorbance at 483 nm.

2.5 Cell expansion

Different types of cells were utilized in this work, including human bone marrow-derived mesenchymal stem cells (MSCs, passage 4) obtained from LONZA (MD, USA), and the human osteosarcoma cell line (MG63) purchased from Procell Life Science & Technology Co., Ltd (China; Catalog No. CL-0157). The MG63 cells were originally established from a 14 year-old Caucasian male with osteosarcoma. The cells were seeded in 175 cm^2 tissue-treated culture flasks and cultured with cell-specific proliferation media in a humidified incubator (5% CO_2, 37 °C). MSCs were cultured in MSCBM™ medium (Lonza, Swiss) and MG63 were cultured in Dulbecco's Modified Eagle's Medium (DMEM, high glucose) supplemented with 10% FBS (Gibco, NY), 100 unit per mL penicillin, 100 μg mL^{-1} streptomycin. When cells reached 70–80% confluence, the sub-cultured cells were obtained using 0.25% trypsin/EDTA (Sigma, USA).

2.6 Characterization

The morphology and composition of nanoparticles were observed *via* transmission electron microscopy (TEM), scanning transmission electron microscopy (STEM) and EDS mapping (JEOL JEM-ARM200F). The samples were prepared according to our previous report. In brief, 5 μL of sample solution was dropped onto a glow-discharged carbon film-coated copper grid.[35] After removal of excess solution, the grid was dried in air.

For scanning electron microscope (SEM) sample preparation, the harvested scaffolds were first washed with PBS three times and then fixed with 2.5% glutaraldehyde for 1 hour at room temperature. The graded ethanol–water solution series (v/v%) (50% ~100% ethanol) was used to dehydrate the fixed samples. Then, the scaffolds were dropped in a graded *tert*-butyl alcohol–ethanol solution (v/v%) (50–100%) to replace ethanol solution. Finally, the harvested scaffolds were freeze-dried for SEM observation. The morphology of scaffolds was characterized using a SEM (JSM-6400Fs; JEOL, Tokyo, Japan) machine with an operating voltage of 3 kV.

2.7 Live and dead assay

For confirmation of the mortality of cells, the viability of MG63 cells was stained by calcein-AM and propidium iodide (PI) staining reagents (Live/Dead Cell Double Staining kit, Beyotime, China). Experiment processes were carried out according to the manufacturer's instruction. In brief, the constructs before and after being cultured in different conditions were immersed in PBS solution suspended with a mixture of 2 μM calcein-AM and 4 μM PI. The incubation was performed at room temperature for 30 minutes. Afterwards, the stained samples were observed using an inverted fluorescence microscope (Leica, Germany).

2.8 Cell uptake of DOX after incubation with hybrid meshes

The MG63 cells were seeded in 24-well culture plates (1×10^4 per well) and cultured with DMEM medium supplemented with 10% FBS (Gibco, NY), 100 unit per mL penicillin, 100 μg mL^{-1} streptomycin. After cell attachment, the PLGA-collagen or DOX-MSNCaP@PLGA-collagen hybrid mesh ($\varphi = 10$ mm) was added to the culture plate and the culture media were further refreshed with DMEM (pH = 7.4 or 6.5). After 12 hours of incubation, the meshes were removed and the cell uptake of DOX was observed using a microscope (Leica). Cell nuclei and F-actin cytoskeleton were stained with Hoechst 33258 (Sigma) and FITC-labeled phalloidin (Sigma).

2.9 DNA laddering assay

MG63 cells were seeded and cultured in 24-well culture plates at the initial cell number 2×10^4 per well. Afterwards, the PLGA-collagen and DOX-MSNCaP@PLGA-collagen hybrid meshes ($\varphi = 10$ mm) were added to each well. The cells were further incubated with DMEM at different pH conditions. After 48 hours of incubation, the hybrid meshes were removed and the supernatants were discarded carefully. The remaining cells were extracted for DNA laddering analysis according to the manufacturer's illustration (Thermo).

2.10. BrdU staining

For BrdU staining, the harvested MG63 cells were plated in 24-well culture plates (1×10^4 per well) and treated with DOX-MSNCaP@PLGA-collagen at different pH conditions. Afterwards, the cells were labeled by the addition of BrdU (10 μM per well) for 2 hours. Cell nuclei and F-actin cytoskeleton were labeled by Hoechst 33258 and FITC-labeled phalloidin, respectively. The constructs were further observed under a fluorescence microscope (Leica).

2.11 YAP staining

The mechanotransdution on MSCs was evaluated by YAP staining. Briefly, after the MSCs were seeded and cultured in PLGA-collagen or DOX-MSNCaP@PLGA-collagen meshes for 1 day, the constructs were washed with PBS twice, followed by being treated with 4% paraformaldehyde and 0.1% Triton X-100. Afterwards, the cells on the meshes were blocked with 2% BSA for 30 minutes and washed with PBS twice. Then, the constructs were further incubated with an anti-YAP primary antibody (Santa Cruz Biotechnology, USA) at 4 °C overnight. After washing with PBS, the constructs were incubated with the second antibody (Alexa Fluor-488 anti-mouse antibody, 1 : 1000 in PBS). Additionally, the cell nucleus and F-actin cytoskeleton were co-stained with Hoechst 33258 and FITC-labeled phalloidin. The fluorescent images were obtained by a fluorescence microscope (Leica). The percentages of YAP nuclei localization were analyzed by calculating the nuclear-cytoplasmic distribution ratio (Nuc/cyto ratio) according to the following equation:

$$\text{Nuc/cyto ratio} = \frac{I_{nuc}/A_{nuc}}{(I_{total} - I_{nuc})/(A_{total} - A_{nuc})}$$

I_{nuc} represents the integrated intensity of YAP fluorescence; A_{nuc} represents the size of nuclear; A_{total} represents the size of the whole cell; I_{total} represents the integrated intensity of YAP fluorescence.

2.12 Real-time PCR assay

The expressed level of osteogenesis-related genes encoding runt-related transcription factor-2 (Runx2), ALP, secreted phosphoprotein 1 (SPP1), and bone sialoprotein 2 (IBSP) were analyzed by real-time PCR. In detail, a TRZOL solution was used to extract the total RNA from the harvest samples. The total RNA was then translated into cDNA using a SuperScript IV VILOTM master mix kit. The real-time PCR analysis was performed using the cDNA as a template, and the analysis was conducted in 25 μL of a reaction system. A comparative C_t method was used to calculate the expression level and the results were normalized to the housekeeping gene (GAPDH). The sequence of all the primers and probes was shown in Table S1.

2.13 Alkaline phosphatase (ALP) and immunochemical staining

ALP staining: the PLGA-collagen and DOX-MSNCaP@PLGA-collagen scaffolds were harvested and their osteogenic differentiation was evaluated through ALP and immunochemical staining. Firstly, the constructs were immersed in ALP staining solution containing 0.1% naphthol AS-MX phosphate (Sigma, St. Louis, MO) and 0.1% fast blue RR salt (Sigma, St. Louis, MO) in 56 mM 2-amino-2-methyl-1,3-propanediol (pH 9.9, Sigma, St. Louis, MO). After 10 minutes of incubation, the constructs were washed with PBS three times, and followed by being observed under an optical microscope (Leica).

Immunochemical staining: immunochemical staining was performed on the PLGA-collagen and DOX-MSNCaP@PLGA-collagen constructs to evaluate the expression of osteogenic markers, following a previously described protocol with minor modifications.[34] Briefly, the constructs were harvested and washed with phosphate-buffered saline (PBS) to remove residual culture media. Samples were fixed in 4% paraformaldehyde (PFA) for 20 minutes at room temperature. To minimize non-specific antibody binding, the fixed samples were blocked with 2% bovine serum albumin (BSA) in PBS for 30 minutes. Following blocking, the constructs were incubated with primary antibodies against collagen type I, fibronectin, and osteocalcin (OCN) (Santa Cruz Biotechnology, CA) at 4 °C overnight. After three consecutive washes with PBS, the samples were incubated with the corresponding HRP-conjugated secondary antibodies for 1 hour at room temperature. Finally, the stained constructs were visualized using an optical microscope. Representative images were acquired from the central regions of the scaffolds to ensure consistent evaluation of protein distribution.

2.14 Statistical analysis

Two-tailed *t*-tests were used to determine the significance between the two groups and a one-way analysis of variance with a Tukey post hoc test was used to analyze multiple groups. The

analysis of data was performed by using GraphPad Prism 7.0 software. Measures are presented as means ± standard deviation (SD).

3 Results and discussion

3.1 Preparation and characterization of DOX-MSNCaP nanoparticles and hybrid scaffolds

DOX-loaded MSNCaP nanoparticles were synthesized *via* a modified established protocol. To optimize drug loading prior to CaP coating, a DOX concentration gradient (0.5–5.0 mg mL^{-1}) was evaluated (Fig. S3 and Table S2). An initial DOX concentration of 2.0 mg mL^{-1} yielded the maximum drug loading efficiency (65.7 ± 2.1%) and a near-saturation drug loading capacity (56.8 ± 1.9%), providing the optimal formulation for all subsequent nanoparticle preparations. TEM imaging revealed the ordered mesoporous structure of MSN (Fig. 1A), which was effectively coated by the CaP layer in MSNCaP (Fig. 1B). DLS analysis indicated a slight increase in particle size from 170.4 ± 29.4 nm (MSN) to 225.1 ± 30.7 nm (MSNCaP) following coating. Concurrently, the zeta potential shifted from −2.7 ± 0.8 mV to 16.4 ± 1.3 mV (Fig. 1C). The successful formation of the CaP shell was further confirmed by elemental mapping, which showed the distribution of calcium and phosphorus (Fig. 1D–I).

For scaffold fabrication, PLGA-collagen scaffolds were prepared according to our previous study,[36] and subsequently hybridized with MSNCaP-embedded collagen sponges to form DOX-MSNCaP@PLGA-collagen constructs. SEM analysis showed that while both groups shared a similar porous macroscopic structure, they differed significantly in microscopic surface morphology (Fig. 1J and K). Specifically, high-magnification views revealed that the smooth pore walls of the PLGA-collagen scaffold contrasted with the rough surfaces observed in the DOX-MSNCaP@PLGA-collagen group. This surface roughness provides evidence of the successful integration of MSNCaP nanoparticles within the scaffold matrix. Because the MSNCaP nanoparticles possess an inorganic CaP shell lacking reactive functional groups for EDC/NHS coupling, they are purely physically entrapped rather than chemically cross-linked to the matrix. Nevertheless, the subsequent chemical cross-linking of the surrounding collagen into

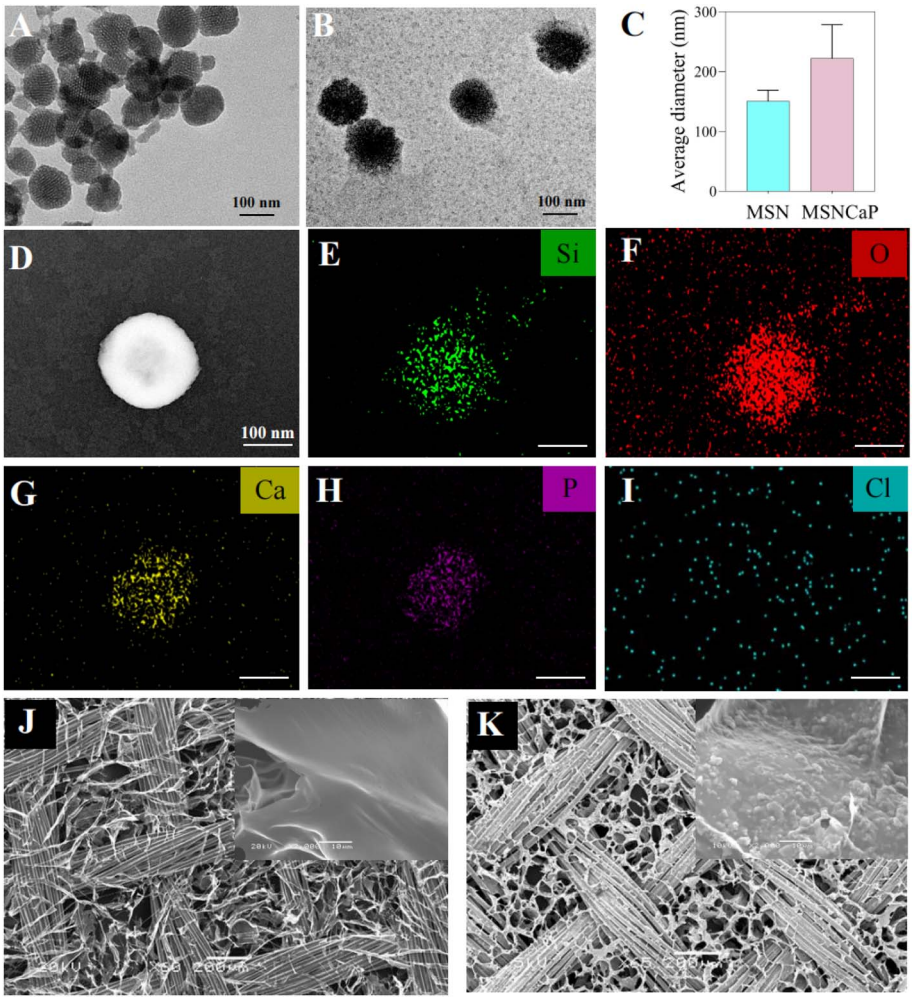

Fig. 1 Structural and compositional characterizations of MSNCaP, PLGA and DOX-MSNCaP@PLGA-collagen scaffolds. Characterization of mesoporous silica nanoparticles (MSN) (A) and calcium phosphate coated MSN (MSNCaP) (B) by TEM. The average diameter of MSN and MSNCaP (C). EDS elemental mapping of MSNCaP (D–I). Representative SEM images of PLGA-collagen (J) and DOX-MSNCaP@PLGA-collagen (K).

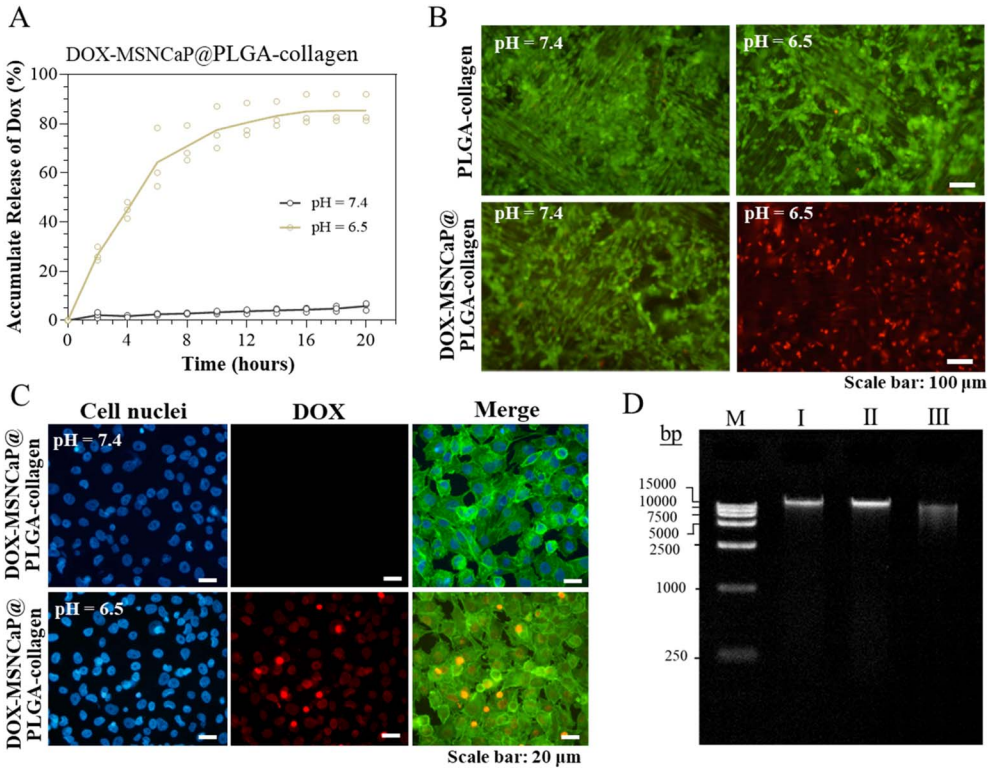

Fig. 2 Biological characterizations of DOX-MSNCaP@PLGA-collagen and PLGA-collagen constructs. The accumulate release of DOX from DOX-MSNCaP@PLGA-collagen in PBS buffer with different pH (A). Cytotoxic assessment of MG63 cells after being cultured in scaffolds *via* live and dead staining. Cells were seed in the meshes and incubated in DMEM at pH 7.4 or pH 6.5 (B). Fluorescence microscopic observation on the intracellular distribution of DOX in MG63 cells after incubation with DOX-MSNCaP@PLGA-collagen scaffolds for 12 hours. Cell nucleus was represented blue fluorescence; DOX was represented red fluorescence; actin cytoskeleton was represented green fluorescence (C). DNA laddering analysis on the severity of DNA fragmentation in MG63 cells upon treatment of DOX-MSNCaP@PLGA-collagen for 12 hours (I: PLGA-collagen at pH 7.4, II: DOX-MSNCaP@PLGA-collagen at pH 7.4, III: DOX-MSNCaP@PLGA-collagen at pH 6.5) (D).

a robust 3D network tightly locks the nanoparticles within the micro-sponges. This stable physical entrapment effectively prevents premature nanoparticle leaching in physiological environments, which is further corroborated by the minimal drug leakage observed at pH 7.4.

3.2 Acid-triggered doxorubicin release and apoptotic induction in MG63 cells

Tumor recurrence is frequently accompanied by the acidification of the local tissue microenvironment. Furthermore, it is well-established that even after surgical tumor resection, the specific post-operative and post-chemotherapy bone defect environment remains weakly acidic.[37,38] Herein, we explored the acid-triggered drug release behavior of the DOX-MSNCaP@PLGA-collagen scaffolds. The release profile of DOX was evaluated in PBS buffer using UV-vis absorbance. As shown in Fig. 2A, DOX release was successfully triggered in weakly acidic PBS, with the release rate gradually decreasing over the incubation period. In contrast to the release profile observed in a neutral environment, the cumulative release of DOX under weakly acidic conditions exceeded 80% within 20 hours. This suggests that the hybrid scaffolds can efficiently release their encapsulated therapeutic payload in response to acidic stimuli.

Subsequently, the *in vitro* anti-tumor efficacy of the scaffolds was assessed under acidic conditions to evaluate their therapeutic potential. MG63 cells were seeded onto the hybrid scaffolds and cultured for 12 hours to allow for cell attachment. The medium was then replaced with DMEM adjusted to pH 6.5 to mimic the weakly acidic tumor microenvironment, and the constructs were cultured for an additional 2 days. Live/dead staining results revealed that MG63 cells seeded on control PLGA-collagen scaffolds remained viable (stained green) at both pH 7.4 and pH 6.5. Conversely, in the DOX-MSNCaP@PLGA-collagen group, almost all tumor cells exhibited extensive cell death (stained red) (pH 6.5) under the mildly acidic conditions (pH 6.5), whereas the majority of cells remained viable when cultured at pH 7 (Fig. 2B).

We further investigated the cellular uptake efficiency of the released DOX *via* a fluorescence microscope. As depicted in Fig. 2C, intense red fluorescence was observed in the cell nuclei when the DOX-MSNCaP@PLGA-collagen constructs were cultured in DMEM at pH 6.5, indicating the effective internalization and nuclear accumulation of the released DOX by the MG63 cells. In contrast, constructs cultured in a neutral pH environment exhibited negligible DOX leakage and minimal nuclear fluorescence. As expected, no red fluorescence was observed in the control PLGA-collagen group (Fig. S1). The

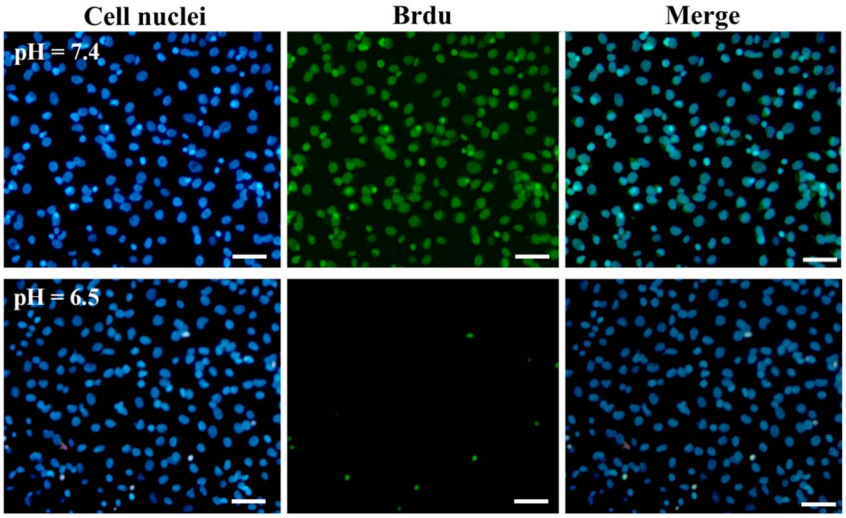

Fig. 3 BrdU staining of MG63 upon treatment of DOX-MSNCaP@PLGA-collagen at pH 7.4 or pH 6.5. Scale bar: 50 μm.

apoptosis-inducing effect on osteosarcoma cells was further confirmed by analyzing DNA fragmentation, a classic hallmark of apoptosis. The results demonstrated that after treatment with DOX-MSNCaP@PLGA-collagen at pH 6.5 for 48 hours, the cells exhibited distinct DNA laddering; notably, this phenomenon was not observed in cells treated at pH 7.4 (Fig. 2D).

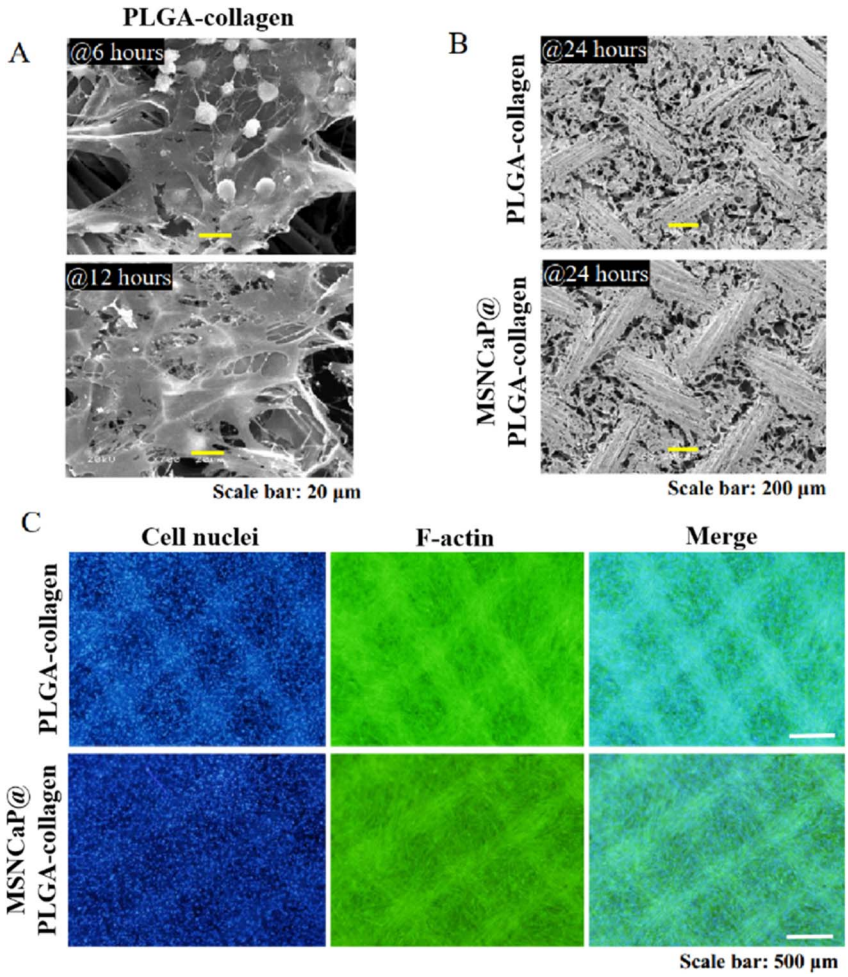

Fig. 4 Culture of MSCs in PLGA-collagen mesh or MSNCaP@PLGA-collagen mesh. Representative SEM images of MSCs in PLGA-collagen or MSNCaP@PLGA-collagen mesh, the cells were cultured in the hybrid mesh for 6, 12 hours (A) and 24 hours (B). The distribution of MSCs in PLGA-collagen or MSNCaP@PLGA-collagen mesh (after 3 days of culture) (C). Blue: cell nuclei; green: F-actin.

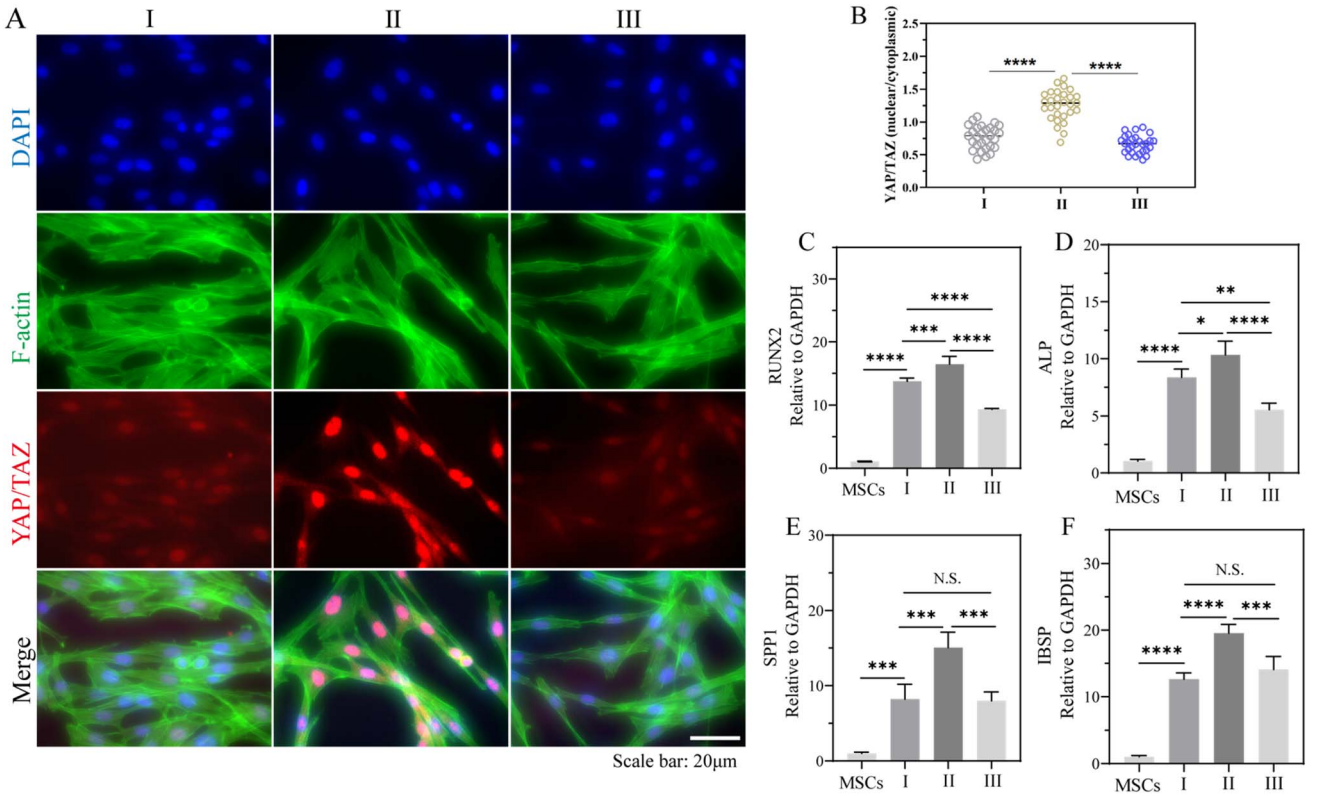

Fig. 5 YAP/TAZ localization and osteogenic gene expression of MSCs. (A) Immunofluorescence staining of F-actin (green), YAP/TAZ (red), and nuclei (DAPI, blue) in MSCs cultured on PLGA-collagen (I), DOX-MSNCaP@PLGA-collagen (II), and DOX-MSNCaP@PLGA-collagen treated with the YAP inhibitor verteporfin (III). (B) Quantification of the nuclear-to-cytoplasmic ratio of YAP/TAZ fluorescence intensity across the three groups. (C–F) Real-time PCR analysis of osteogenesis-related genes, including RUNX2 (C), ALP (D), SPP1 (E), and IBSP (F). Data in (C–F) are normalized to the gene expression of sub-cultured MSCs prior to seeding. All data are presented as mean ± SD ($n = 4$). *$p < 0.05$, **$p < 0.01$, ***$p < 0.001$, ****$p < 0.0001$; N.S., not significant.

Finally, DNA synthesis activity, a critical indicator of cancer cell proliferation,[39] was investigated using BrdU incorporation assays (Fig. 3 and S2). MG63 cells cultured on DOX-MSNCaP@PLGA-collagen scaffolds in a neutral environment showed extensive green staining, indicating high proliferative activity, comparable to cells cultured on the control PLGA-collagen scaffolds at both pH 7.4 and 6.5. However, when the culture environment was switched to mildly acidic conditions, a drastic reduction in BrdU-positive cells was observed in the drug-loaded scaffold group. These results confirm that the mildly acidic environment effectively triggers the release of DOX from the DOX-MSNCaP@PLGA-collagen scaffolds, thereby efficiently eliminating cancer cells and inhibiting their proliferation.

3.3 Evaluation of MSC adhesion on DOX-MSNCaP@PLGA-collagen scaffolds

To assess the suitability of the therapeutic scaffold for stem cell recruitment, we examined the initial adhesion and spreading of MSCs. Observations revealed that MSCs firmly attached to the scaffold surface after 6 hours and transitioned to a stretched, spindle-like morphology by 12 hours (Fig. 4A). Following 24 hours of culture, the constructs presented a significantly reduced porous appearance compared to cell-free scaffolds, indicating extensive cell infiltration and pore occupancy (Fig. 4B, 1J and K). Furthermore, cell staining revealed a homogeneous distribution of MSCs throughout the hybrid scaffolds. Cytoskeletal analysis confirmed a well-spread morphology with organized actin filaments in both the PLGA-collagen and DOX-MSNCaP@PLGA-collagen groups (Fig. 4C), suggesting excellent biocompatibility and a surface environment conducive to cell attachment.

3.4 Mechanotransduction-mediated YAP activation and promotion of osteogenic differentiation

Cells possess the intrinsic ability to sense physical microenvironments and convert mechanical stimuli into biochemical signals through a process known as mechanotransduction. Yes-associated protein (YAP) and transcriptional coactivator with PDZ-binding motif (TAZ) act as nuclear mechanosensors, playing pivotal roles in regulating the Hippo signaling pathway.[40] Furthermore, recent evidence identifies YAP activation as a key driver in Wnt signaling-mediated osteogenic differentiation.[41–43] Given that the simulated post-chemotherapy tumor microenvironment in this study exhibits a rougher surface topography (attributed to the incorporated MSNCaP nanoparticles), we hypothesized that the scaffold could enhance MSC activity

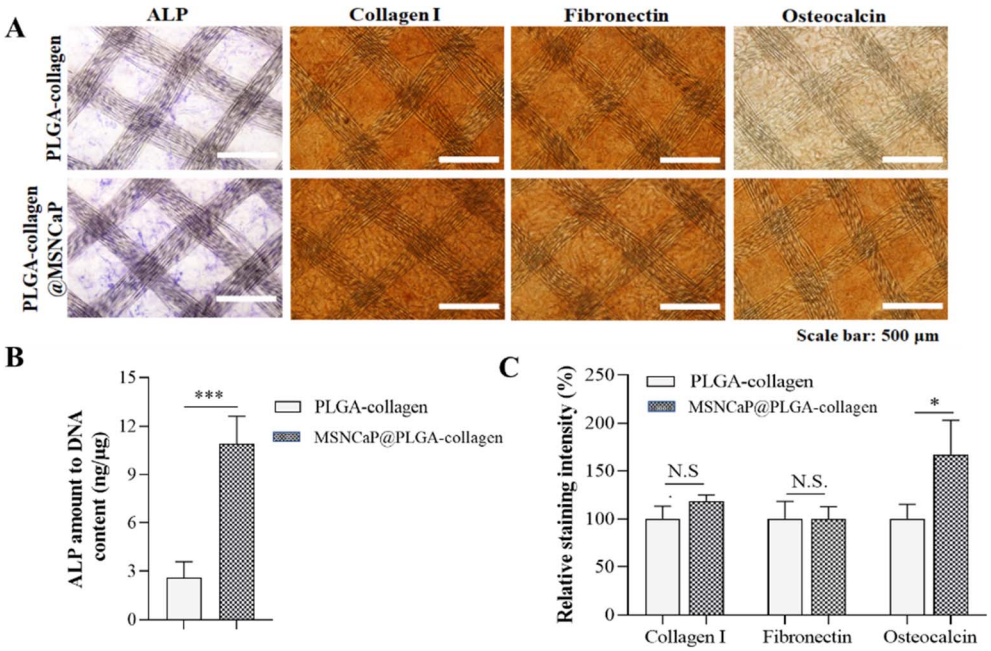

Fig. 6 ALP activity and immunohistochemical staining were performed to analyze collagen I, fibronectin, and osteocalcin in the cells/PLGA-collagen or cells/DOX-MSNCaP@PLGA-collagen constructs (A). The ALP activity was quantitatively analyzed (B). The immunocytochemical staining intensity was quantitatively analyzed and normalized to the level of collagen I, fibronectin, or osteocalcin in the PLGA-collagen scaffold (C). All cellular-scaffold constructs were cultured for a period of 21 days.

within this specific niche through mechanotransduction pathways.

To explore this mechanism and definitively establish the causal role of YAP-mediated mechanotransduction, we performed YAP immunofluorescence staining on MSCs, including a group treated with the specific YAP pharmacological inhibitor verteporfin (VP). As depicted in Fig. 5A, cells cultured on the DOX-MSNCaP@PLGA-collagen scaffold (Group II) exhibited a well-spread, spindle-shaped morphology with distinct nuclear translocation of YAP. In contrast, cells cultured on the control PLGA-collagen scaffold (Group I) showed minimal YAP nuclear localization. Crucially, the addition of VP (Group III) successfully blocked this topography-induced YAP nuclear entry. Quantitative analysis of the YAP distribution (Fig. 5B) further corroborated these observations, revealing a marked increase in the nuclear-to-cytoplasmic YAP ratio in the DOX-MSNCaP@PLGA-collagen group, which was significantly reversed following VP treatment.

To further validate whether this YAP activation directly dictates downstream osteogenic effects at the transcriptional level, real-time PCR was employed to quantify the expression of key osteogenesis-related genes, including RUNX2, ALP, SPP1, and IBSP. MSCs on the DOX-MSNCaP@PLGA-collagen scaffold exhibited a robust upregulation of these genes compared to the PLGA-collagen control. However, following the pharmacological inhibition of YAP with VP, this topography-driven genetic upregulation was significantly abrogated (Fig. 5C–F). This direct downregulation provides definitive functional evidence that the enhanced osteogenic differentiation triggered by the nanostructured scaffold is intrinsically dependent on the YAP signaling pathway. Subsequently, osteogenic differentiation was assessed at the protein level. Consistent with the gene expression data, cells on the DOX-MSNCaP@PLGA-collagen scaffold displayed higher ALP staining intensity and enzymatic activity (Fig. 6A and B).

Immunocytochemical staining was performed to visualize dominant extracellular matrix (ECM) components, specifically collagen I, fibronectin, and osteocalcin (Fig. 6A and C). While collagen I was robustly expressed in both groups, distinct differences were observed in fibronectin and osteocalcin expression. Previous literature suggests that lower fibronectin density favors osteogenic differentiation in MSCs.[44] Consistent with this, the DOX-MSNCaP@PLGA-collagen scaffold exhibited weaker fibronectin staining compared to the strong signal observed in the PLGA-collagen group. Conversely, osteocalcin, a critical regulator of bone mineralization,[45] showed intense staining in the DOX-MSNCaP@PLGA-collagen group but only weak expression in the control. This indicates that the incorporation of MSNCaP significantly enhances the osteogenic potential of the scaffold. Collectively, we successfully fabricated a DOX-MSNCaP@PLGA-collagen hybrid scaffold to simulate the residual post-chemotherapy tumor microenvironment *in vitro*. Our investigation demonstrates that this specific biomimetic environment effectively promotes the subsequent osteogenic differentiation of MSCs *via* mechanotransduction.

In this study, we established a biomimetic system to simulate the post-chemotherapy tumor microenvironment *in vitro*. Unlike conventional scaffold studies that evaluate biocompatibility purely in ideal physiological conditions, or existing bifunctional platforms that attempt to merge tumor ablation and regeneration simultaneously, our model uniquely incorporates the critical elements of realistic sequential cancer

therapy: acidic pH and the presence of residual chemotherapeutic agents (DOX). The pH-responsive release profile of DOX from the MSNCaP nanoparticles (Fig. 2) effectively mimics the local acidification and drug accumulation often observed in tumor recurrence or post-treatment sites. This hostile environment typically inhibits cell proliferation; however, our results surprisingly demonstrated that MSCs could maintain viability and undergo robust osteogenic differentiation within this simulated environment. This suggests that specific cues within the scaffold can counteract the negative impact of chemical stressors. The most significant finding of this work is the pivotal role of mechanotransduction in driving osteogenesis, even under chemotherapeutic stress. While chemotherapy is generally detrimental to stem cell function, our data indicates that the physical architecture of the scaffold plays a compensatory protective role. The incorporation of MSNCaP nanoparticles created a hierarchical nano-roughness on the PLGA-collagen pore walls (Fig. 1), which acted as a potent physical cue.

Our mechanistic investigation revealed that this surface topography triggered the activation of the YAP signaling pathway. As shown in Fig. 5 and 6, MSCs on the hybrid scaffold exhibited distinct nuclear translocation of YAP, a hallmark of mechanotransduction-mediated osteogenesis. We propose that the strong mechanical signaling provided by the rough nanotopography overrides the inhibitory chemical signals from the DOX/acidic environment.[46,47] Consequently, the activated YAP pathway induces the transcriptional upregulation of critical osteogenic markers (RUNX2, ALP, and OCN), which facilitates osteogenesis.

The ability of the DOX-MSNCaP@PLGA-collagen scaffold to induce osteogenesis in a simulated post-chemotherapy environment offers a new perspective on scaffold design. It implies that for post-tumor reconstruction, material design should not only focus on drug delivery efficiency but also on providing strong physical cues (like nanotopography) to "rescue" stem cells from the harsh microenvironment.[48,49] This study validates the concept that modulating the biophysical properties of the implant surface is a viable strategy to enhance regeneration in pathological, drug-laden tissue environments.[50–52]

4 Conclusion

In conclusion, our investigation into the simulated post-chemotherapy niche highlights nanotopography-driven mechanotransduction as a key determinant in sustaining MSC viability and differentiation functionality. We proved that surface topography can effectively counterbalance the osteogenic inhibition caused by chemotherapeutic agents. This study not only provides mechanistic insights into cell-material interactions under stress conditions but also offers a robust strategy for the development of bifunctional implants capable of integrating oncological therapy with regenerative medicine.

Conflicts of interest

The authors declare that they have no competing interests.

Data availability

All data generated or analyzed during this study are included in this article and its supplementary information (SI). Supplementary information: supporting data on material characterization and *in vitro* cellular assays. Data regarding the fluorescence microscopic evaluations of intracellular DOX distribution (Fig. S1) and BrdU cell proliferation assays under varying pH conditions (Fig. S2) in MG63 cells are presented. Additionally, primers and probes for real-time PCR analysis are listed in Table S1. Optimization and characterization of doxorubicin (DOX) loading efficiency and capacity in mesoporous silica nanoparticles (MSNs) are included (Fig. S3 and Table S2). See DOI: https://doi.org/10.1039/d6ra01031h.

Acknowledgements

This work was supported by the Anhui Provincial Special Program for Translational Research in Clinical Medicine (202304295107020118), the Henan Science and Technology R&D Program Joint Funds Young Scientist Project (No. 245200810107), and the Henan Charity Federation Daojian Fund General Project (No. szsyky24017).

References

1 H. C. Beird, S. S. Bielack, A. M. Flanagan, J. Gill, D. Heymann, K. A. Janeway, J. A. Livingston, R. D. Roberts, S. J. Strauss and R. O. Gorlick, *Nat. Rev. Dis. Primers*, 2022, **8**(1), 77, DOI: 10.1038/s41572-022-00409-y.

2 X. Zhao, G. Shan, D. Xing, H. Gao, Z. Xiong, W. Hui and M. Gong, Interfering with UBE2L3 Expression Targets Regulation of MLKL to Promote Necroptosis Inhibition of Growth in Osteosarcoma, *World J. Surg. Oncol.*, 2025, **23**(1), 63, DOI: 10.1186/s12957-025-03715-3.

3 R. Shen, M. Chen, X. Zhu and J. Lin, Aging Reshapes the Osteosarcoma Ecosystem through Immune Dysfunction and Tumor Cell Reprogramming, *Cell. Oncol.*, 2026, **49**(1), 26, DOI: 10.1007/s13402-026-01162-0.

4 S. S. Bielack, D. Andreou, D. Baumhoer, C. Blattmann, G. Friedel, B. Fröhlich, S. B. Harrabi, L. Kager, T. von Kalle, T. Kessler, M. Kevric, A. Knoll, T. Kühne, P. Reichardt, B. Sorg, R. Windhager and S. Hecker-Nolting, Undifferentiated Pleomorphic Sarcoma of Bone (UPSB) Treated in the German-Speaking Countries. A Report of 132 Unselected Patients from the Cooperative Osteosarcoma Study Group (COSS), *J. Cancer Res. Clin. Oncol.*, 2026, **152**(1), 40, DOI: 10.1007/s00432-025-06405-5.

5 Y. Dreznik, C. Sher, A. Baazuv, G. Yekutiel and D. Kravarusic, Recurrence Rates of Pilonidal Sinus Disease in the Pediatric Population Following Trephine Surgery, *World J. Surg.*, 2024, **48**(5), 1261–1265, DOI: 10.1002/wjs.12167.

6 D. Doll, S. Haas, I. K. Faurschou, T. Hackmann, H. Heitmann, M. Braun-Münker and C. Oetzmann von Sochaczewski, Pediatric Pilonidal Sinus Disease: Recurrence Rates of Different Age Groups Compared to

Adults, *Surg. Open Sci.*, 2025, **23**, 50–56, DOI: 10.1016/j.sopen.2025.01.001.

7 N. Nosalova, M. Huniadi, Ľ. Horňáková, A. Valenčáková, S. Horňák, K. Nagoos, J. Vozar and D. Cizkova, Canine Mammary Tumors: Classification, Biomarkers, Traditional and Personalized Therapies, *Int. J. Mol. Sci.*, 2024, **25**(5), 2891, DOI: 10.3390/ijms25052891.

8 R. Kaur, A. Bhardwaj and S. Gupta, Cancer Treatment Therapies: Traditional to Modern Approaches to Combat Cancers, *Mol. Biol. Rep.*, 2023, **50**(11), 9663–9676, DOI: 10.1007/s11033-023-08809-3.

9 D. Barik and V. B. Konkimalla, Next-Generation Nanomaterials in Biology: From Tissue Regeneration to Targeted Cancer Therapy, *IUBMB Life*, 2025, **77**(11), e70071, DOI: 10.1002/iub.70071.

10 J. S. Kim, H. Nam, E. C. Kim, H. J. Jeong and S. J. Lee, Bioengineered Approaches for Esophageal Regeneration: Advancing Esophageal Cancer Therapy, *Bioengineering*, 2025, **12**(5), 479, DOI: 10.3390/bioengineering12050479.

11 G. Shi, S. Lan, Q. Zhang, J. Wang, F. Shu, Z. Hao, T. Chen, M. Zhu, R. Chen, J. Chen, Z. Wu, B. Wu, Z. Zou and J. Li, Molybdenum Nanodots Act as Antioxidants for Photothermal Therapy Osteoarthritis, *Biomaterials*, 2025, **315**, 122909, DOI: 10.1016/j.biomaterials.2024.122909.

12 R. Sun, M. Wang, T. Zeng, H. Chen, T. Yoshitomi, M. Takeguchi, N. Kawazoe, Y. Yang and G. Chen, Scaffolds Functionalized with Matrix Metalloproteinase-Responsive Release of miRNA for Synergistic Magnetic Hyperthermia and Sensitizing Chemotherapy of Drug-Tolerant Breast Cancer, *Bioact. Mater.*, 2025, **44**, 205–219, DOI: 10.1016/j.bioactmat.2024.10.011.

13 X. Liu, H. Chen, M. Wang, T. Zeng, T. Yoshitomi, N. Kawazoe, Y. Yang and G. Chen, Thermosensitive Liposomal Nanomedicine-Functionalized Photothermal Composite Scaffolds for Light-Guided Cancer Therapy, *Mater. Horiz.*, 2025, **12**(20), 8654–8666, DOI: 10.1039/d5mh00888c.

14 Y. He, C. Lv, N. Le Breton, H. Peng, T. Wang, P. Samorì, S. Choua, A. Bianco, B. Ma and C. Ménard-Moyon, A Co-Catalytic Nanosystem Based on Molybdenum Disulfide and Prussian Blue for Synergistic Chemodynamic and Photothermal Therapy through Mitochondrial Damage and Ferroptosis, *Acta Biomater.*, 2025, **204**, 518–533, DOI: 10.1016/j.actbio.2025.07.037.

15 Y. Han, H. Wei, Q. Ding, C. Ding and S. Zhang, Advances in Electrospun Nanofiber Membranes for Dermatological Applications: A Review, *Molecules*, 2024, **29**(17), 4271, DOI: 10.3390/molecules29174271.

16 L. Sutrisno, H. Chen, Y. Chen, T. Yoshitomi, N. Kawazoe, Y. Yang and G. Chen, Composite Scaffolds of Black Phosphorus Nanosheets and Gelatin with Controlled Pore Structures for Photothermal Cancer Therapy and Adipose Tissue Engineering, *Biomaterials*, 2021, **275**, 120923, DOI: 10.1016/j.biomaterials.2021.120923.

17 X. Liu, J. Xu, J. Zhu, Z. Wang, H. Fang, W. Guo, L. Cao, Y. Y. Cheng and K. Song, Multimodal Therapy Process Engineering Mediated by 3D-Printed Scaffolds for Enhanced Postoperative Osteosarcoma Regeneration, *Tissue Cell*, 2026, **98**, 103212, DOI: 10.1016/j.tice.2025.103212.

18 J. H. Dong, Y. Ma, R. Li, W. T. Zhang, M. Q. Zhang, F. N. Meng, K. Ding, H. T. Jiang and Y. K. Gong, Smart MSN-Drug-Delivery System for Tumor Cell Targeting and Tumor Microenvironment Release, *ACS Appl. Mater. Interfaces*, 2021, **13**(36), 42522–42532, DOI: 10.1021/acsami.1c14189.

19 J. Wang, H. Sun, L. Wang, W. Wang and H. Long, Preparation of Mesoporous Silica Nanoparticles with Ordered Mesopores in High Silica Content Templating System Assisted by a Pre-Hydrolysis Step, *J. Non-Cryst. Solids*, 2026, **677**, 123979, DOI: 10.1016/j.jnoncrysol.2026.123979.

20 D. S. Ghallab, D. A. Ghareeb, M. Sherif and M. Y. Kenawy, Systematic Evaluation of a Novel Mesoporous Silica Nanoparticles (MSNs)-Spirulina Platensis Nanohybrid for Breast Cancer Treatment: Mechanistic Investigation *via* Pharmacological Network Analysis, *RSC Adv.*, 2026, **16**(5), 4347–4362, DOI: 10.1039/d5ra08876c.

21 S. Porrang, G. Baran and N. Mustafaoglu, Green Synthesized Mesoporous Silica Nanoparticles Offer a Promising Drug Delivery System Investigated in Physiologically Relevant 3D Microfluidic Models, *RSC Adv.*, 2025, **15**(49), 42071–42086, DOI: 10.1039/d5ra06132f.

22 F. Yuan, L. Wang, L. Ning, J. Zhang and Y. Guo, Gas-Mediated Reinforcement of Cancer Therapies: Emerging Strategies and Future Perspectives, *Chem. Sci.*, 2025, **16**(43), 20108–20123, DOI: 10.1039/d5sc04798f.

23 W. Fan, B. C. Yung and X. Chen, Stimuli-Responsive NO Release for On-Demand Gas-Sensitized Synergistic Cancer Therapy, *Angew. Chem., Int. Ed.*, 2018, **57**(28), 8383–8394, DOI: 10.1002/anie.201800594.

24 Y. He, B. Zeng, S. Liang, M. Long and H. Xu, Synthesis of pH-Responsive Biodegradable Mesoporous Silica–Calcium Phosphate Hybrid Nanoparticles as a High Potential Drug Carrier, *ACS Appl. Mater. Interfaces*, 2017, **9**(51), 44402–44409, DOI: 10.1021/acsami.7b16787.

25 A. D. Trofimov, A. A. Ivanova, M. V. Zyuzin and A. S. Timin, Porous Inorganic Carriers Based on Silica, Calcium Carbonate and Calcium Phosphate for Controlled/Modulated Drug Delivery: Fresh Outlook and Future Perspectives, *Pharmaceutics*, 2018, **10**(4), 167, DOI: 10.3390/pharmaceutics10040167.

26 M. J. Dewey, A. V. Nosatov, K. Subedi, R. Shah, A. Jakus and B. A. C. Harley, Inclusion of a 3D-Printed Hyperelastic Bone Mesh Improves Mechanical and Osteogenic Performance of a Mineralized Collagen Scaffold, *Acta Biomater.*, 2021, **121**, 224–236, DOI: 10.1016/j.actbio.2020.11.028.

27 V. De Gregorio, M. Barua and R. Lennon, Collagen Formation, Function and Role in Kidney Disease, *Nat. Rev. Nephrol.*, 2025, **21**(3), 200–215, DOI: 10.1038/s41581-024-00902-5.

28 H. P. Bächinger and S. P. Boudko, Mysteries of the Collagen Triple Helix, *Matrix Biol.*, 2025, **137**, 12–18, DOI: 10.1016/j.matbio.2025.02.003.

29 Z. Fan, M. Li, K. Cai, Z. Xie, B. Lu, M. Zhang, Y. Zhang, J. Wang, C. Gu, K. Zheng and T. Chen, Flexible Bioactive Glass-Fiber-Reinforced Recombinant Collagen Sponge for Versatile Hemostasis, Antibacterial Protection, and Functional Skin Regeneration, *Adv. Healthcare Mater.*, 2026, e04908, DOI: 10.1002/adhm.202504908.

30 Y. Chen, K. Lee, N. Kawazoe, Y. Yang and G. Chen, ECM Scaffolds Mimicking Extracellular Matrices of Endochondral Ossification for the Regulation of Mesenchymal Stem Cell Differentiation, *Acta Biomater.*, 2020, **114**, 158–169, DOI: 10.1016/j.actbio.2020.07.049.

31 Y. Chen, K. Lee, N. Kawazoe, Y. Yang and G. Chen, PLGA–Collagen–ECM Hybrid Scaffolds Functionalized with Biomimetic Extracellular Matrices Secreted by Mesenchymal Stem Cells during Stepwise Osteogenesis-Co-Adipogenesis, *J. Mater. Chem. B*, 2019, **7**(45), 7195–7206, DOI: 10.1039/C9TB01959F.

32 Y. Chen; K. Lee; Y. Yang; N. Kawazoe; G. J. B. Chen PLGA-Collagen-ECM Hybrid Meshes Mimicking Stepwise Osteogenesis and Their Influence on the Osteogenic Differentiation of hMSCs. 2020, **12** (2), 025027.

33 M. Shi, Y. Zhou, J. Shao, Z. Chen, B. Song, J. Chang, C. Wu and Y. Xiao, Stimulation of Osteogenesis and Angiogenesis of hBMSCs by Delivering Si Ions and Functional Drug from Mesoporous Silica Nanospheres, *Acta Biomater.*, 2015, **21**, 178–189, DOI: 10.1016/j.actbio.2015.04.019.

34 Y. Chen, K. Lee, Y. Yang, N. Kawazoe and G. Chen, PLGA-Collagen-ECM Hybrid Meshes Mimicking Stepwise Osteogenesis and Their Influence on the Osteogenic Differentiation of hMSCs, *Biofabrication*, 2020, **12**(2), 025027, DOI: 10.1088/1758-5090/ab782b.

35 C. Jin, G. Li, X. Wu, J. Liu, W. Wu, Y. Chen, T. Sasaki, H. Chao and Y. Zhang, Robust Packing of a Self-Assembling Iridium Complex *via* Endocytic Trafficking for Long-Term Lysosome Tracking, *Angew Chem. Int. Ed. Engl.*, 2021, **60**(14), 7597–7601, DOI: 10.1002/anie.202015913.

36 Y. Chen, K. Lee, Y. Chen, Y. Yang, N. Kawazoe and G. Chen, Preparation of Stepwise Adipogenesis-Mimicking ECM-Deposited PLGA–Collagen Hybrid Meshes and Their Influence on Adipogenic Differentiation of hMSCs, *ACS Biomater. Sci. Eng.*, 2019, **5**(11), 6099–6108, DOI: 10.1021/acsbiomaterials.9b00866.

37 J. C. Berkmann, A. X. Herrera Martin, A. Ellinghaus, C. Schlundt, H. Schell, E. Lippens, G. N. Duda, S. Tsitsilonis and K. Schmidt-Bleek, Early pH Changes in Musculoskeletal Tissues upon Injury—Aerobic Catabolic Pathway Activity Linked to Inter-Individual Differences in Local pH, *Int. J. Mol. Sci.*, 2020, **21**(7), 2513, DOI: 10.3390/ijms21072513.

38 S. Kang, D. Lee, B. E. Theusch, C. J. Arpey and T. J. Brennan, Wound Hypoxia in Deep Tissue after Incision in Rats, *Wound Repair Regen.*, 2013, **21**(5), 730–739, DOI: 10.1111/wrr.12081.

39 Y. Wang, Y. Chen, C. Wang, M. Yang, Y. Wang, L. Bao, J. E. Wang, B. Kim, K. Y. Chan, W. Xu, E. Capota, J. Ortega, D. Nijhawan, G. M. Li, W. Luo and Y. Wang, MIF Is a 3' Flap Nuclease That Facilitates DNA Replication and Promotes Tumor Growth, *Nat. Commun.*, 2021, **12**(1), 2954, DOI: 10.1038/s41467-021-23264-z.

40 O. Ritsvall and S. Albinsson, Emerging Role of YAP/TAZ in Vascular Mechanotransduction and Disease, *Microcirculation*, 2024, **31**(4), e12838, DOI: 10.1111/micc.12838.

41 L. Wang, Q. Ren, S. Chen, L. Lou, X. Hu, W. Xing, J. Suo, J. Sun, M. B. Greenblatt, H. Feng and W. Zou, Piezo1 Balances the Osteogenic-Tenogenic Plasticity of Periosteal Progenitor Cells through the YAP Pathway, *Cell Rep.*, 2025, **44**(5), 115630, DOI: 10.1016/j.celrep.2025.115630.

42 G. Zhong, S. Su, J. Li, H. Zhao, D. Hu, J. Chen, S. Li, Y. Lin, L. Wen, X. Lin, G. Xian, D. Xu and Q. Zeng, Activation of Piezo1 Promotes Osteogenic Differentiation of Aortic Valve Interstitial Cell through YAP-Dependent Glutaminolysis, *Sci. Adv.*, 2023, **9**(22), eadg0478, DOI: 10.1126/sciadv.adg0478.

43 J. Na, Z. Yang, Q. Shi, C. Li, Y. Liu, Y. Song, X. Li, L. Zheng and Y. Fan, Extracellular Matrix Stiffness as an Energy Metabolism Regulator Drives Osteogenic Differentiation in Mesenchymal Stem Cells, *Bioact. Mater.*, 2024, **35**, 549–563, DOI: 10.1016/j.bioactmat.2024.02.003.

44 A. B. Faia-Torres, T. Goren, T. O. Ihalainen, S. Guimond-Lischer, M. Charnley, M. Rottmar, K. Maniura-Weber, N. D. Spencer, R. L. Reis, M. Textor and N. M. Neves, Regulation of Human Mesenchymal Stem Cell Osteogenesis by Specific Surface Density of Fibronectin: A Gradient Study, *ACS Appl. Mater. Interfaces*, 2015, **7**(4), 2367–2375, DOI: 10.1021/am506951c.

45 F. Wu, C. Ge, H. Pan, Y. Han, Y. Mishina, V. Kaartinen and R. T. Franceschi, Discoidin Domain Receptor 2 Is an Important Modulator of BMP Signaling during Heterotopic Bone Formation, *Bone Res.*, 2025, **13**(1), 7, DOI: 10.1038/s41413-024-00391-z.

46 W. Zhang, S. Liu, Y. Hou, S. Xu, J. An, K. Lee, Q. Miao, N. Wang, Y. Wang and M. Ma, Functional Nanoplatform for Modulating Cellular Forces to Enhance Antitumor Immunity *via* Mechanotransduction, *J. Contr. Release*, 2025, **379**, 850–865, DOI: 10.1016/j.jconrel.2025.01.065.

47 N. Xie, C. Xiao, Q. Shu, B. Cheng, Z. Wang, R. Xue, Z. Wen, J. Wang, H. Shi, D. Fan, N. Liu and F. Xu, Cell Response to Mechanical Microenvironment Cues *via* Rho Signaling: From Mechanobiology to Mechanomedicine, *Acta Biomater.*, 2023, **159**, 1–20, DOI: 10.1016/j.actbio.2023.01.039.

48 D. Xie, C. Hu, Y. Zhu, J. Yao, J. Li, J. Xia, L. Ye, Y. Jin, S. Jiang, T. Hu, J. Lu, H. Song, P. Tang, J. Dai, Y. Xi and Z. Hu, Sequential Therapy for Osteosarcoma and Bone Regeneration *via* Chemodynamic Effect and Cuproptosis Using a 3D-Printed Scaffold with TME-Responsive Hydrogel, *Small*, 2025, **21**(5), e2406639, DOI: 10.1002/smll.202406639.

49 L. Wang, Z. Dai, J. Bi, Y. Chen, Z. Wang, Z. Sun, Z. Ji, H. Wang, Y. Zhang, L. Wang, J. Mao and J. Yang, Polydopamine-Functionalized Calcium-Deficient Hydroxyapatite 3D-Printed Scaffold with Sustained Doxorubicin Release for Synergistic Chemo-Photothermal

Therapy of Osteosarcoma and Accelerated Bone Regeneration, *Mater. Today Bio*, 2024, **29**, 101253, DOI: 10.1016/j.mtbio.2024.101253.

50 M. Shen, Y. Hou, S. Xu, J. Tan, H. Zhou, Q. Miao, W. Zhang, Y. Chen, N. Wang and Y. Wang, Biofunctionalized Patterned Platform as Microarray Biochip to Supervise Delivery and Expression of pDNA Nanolipoplexes in Stem Cells *via* Mechanotransduction, *J. Nanobiotechnol.*, 2025, **23**(1), 22, DOI: 10.1186/s12951-025-03101-x.

51 J. Yang, P. Wang, Y. Zhang, M. Zhang, Q. Sun, H. Chen, L. Dong, Z. Chu, B. Xue, W. D. Hoff, C. Zhao, W. Wang, Q. Wei and Y. Cao, Photo-Tunable Hydrogels Reveal Cellular Sensing of Rapid Rigidity Changes through the Accumulation of Mechanical Signaling Molecules, *Cell Stem Cell*, 2025, **32**(1), 121–136, DOI: 10.1016/j.stem.2024.09.016.

52 X. Liu, M. Zhang, P. Wang, K. Zheng, X. Wang, W. Xie, X. Pan, R. Shen, R. Liu, J. Ding and Q. Wei, Nanoscale Distribution of Bioactive Ligands on Biomaterials Regulates Cell Mechanosensing through Translocation of Actin into the Nucleus, *Proc. Natl. Acad. Sci. U. S. A.*, 2025, **122**(10), e2501264122, DOI: 10.1073/pnas.2501264122.